

Formalizing the Sampling Design Space of Diffusion-Based Generative Models via Adaptive Solvers and Wasserstein-Bounded Timesteps

Sangwoo Jo¹ Sungjoon Choi¹

Abstract

Diffusion-based generative models have achieved remarkable performance across various domains, yet their practical deployment is often limited by high sampling costs. While prior work focuses on training objectives or individual solvers, the holistic design of sampling, specifically solver selection and scheduling, remains dominated by static heuristics. In this work, we revisit this challenge through a geometric lens, proposing **SDM**, a principled framework that aligns the numerical solver with the intrinsic properties of the diffusion trajectory. By analyzing the ODE dynamics, we show that efficient low-order solvers suffice in early high-noise stages while higher-order solvers can be progressively deployed to handle the increasing non-linearity of later stages. Furthermore, we formalize the scheduling by introducing a Wasserstein-bounded optimization framework. This method systematically derives adaptive timesteps that explicitly bound the local discretization error, ensuring the sampling process remains faithful to the underlying continuous dynamics. Without requiring additional training or architectural modifications, **SDM** achieves state-of-the-art performance across standard benchmarks, including an FID of 1.93 on CIFAR-10, 2.41 on FFHQ, and 1.98 on AFHQv2, with a reduced number of function evaluations compared to existing samplers. Our code is available at <https://github.com/aiimaginglab/sdm>.

1. Introduction

Diffusion-based generative models have established themselves as the premier framework for high-fidelity synthesis, defining the state-of-the-art in image generation (Ho et al.,

¹Department of Artificial Intelligence, Korea University, Seoul, South Korea. Correspondence to: Sungjoon Choi <sungjoonc@korea.ac.kr>.

Preprint. February 16, 2026.

2020; Song et al., 2020; Rombach et al., 2022), video synthesis (Ho et al., 2022; Singer et al., 2022), and 3D content creation (Poole et al., 2022; Lin et al., 2023). Fundamentally, these models cast generation as a differential equation problem: sampling is equivalent to numerically integrating a Probability Flow ODE (PF-ODE) that transports a simple prior distribution to the complex data distribution.

However, this theoretical elegance comes with a practical bottleneck. To minimize discretization error, the ODE must be simulated with fine-grained steps, leading to prohibitively high computational costs (measured in Number of Function Evaluations, NFE). While distillation methods (Salimans & Ho, 2022; Meng et al., 2023) and Consistency Models (Song et al., 2023; Luo et al., 2023; Wang et al., 2024; Kim et al., 2023; Yang et al., 2024) offer few-step generation, they require expensive retraining or fine-tuning pipelines. For the vast majority of pre-trained models, the central challenge remains: *How can we solve the generative ODE as efficiently as possible without modifying the model itself?*

Current approaches to this integration problem are largely dominated by static heuristics. Standard solvers (e.g., Euler, Heun) and schedules (e.g., linear, log-SNR, EDM (Karras et al., 2022)) treat the diffusion trajectory as homogeneous, applying the same numerical precision and step-size logic from start to finish. This ignores a critical geometric reality: the stiffness of the diffusion ODE is not constant. As we demonstrate in this work, the trajectory evolves from a nearly linear flow in high-noise regions (dominated by the prior) to a highly non-linear, curved path as it converges onto the low-dimensional data manifold. Treating these distinct regimes with a uniform strategy is inherently suboptimal.

In this work, we formalize the sampling design space through a geometric lens, proposing **SDM**, a principled framework that adapts the numerical solver and schedule to the intrinsic properties of the diffusion trajectory. Our contributions are two-fold:

(i) Curvature Analysis and Solver Allocation. We provide a rigorous analysis of the PF-ODE curvature under standard parameterizations. As illustrated in Figure 1, the trajectory curvature is negligible during early sampling stages but spikes significantly near the data manifold ($t \rightarrow 0$).

Based on this, we propose a dynamic allocation strategy that deploys efficient first-order solvers early and transitions to stable higher-order solvers only when geometrically required. We provide theoretical justification for this solver allocation strategy and empirically validate its effectiveness in Section 4.

(ii) Wasserstein-Bounded Adaptive Scheduling. Moving beyond heuristic timestep selection, we introduce an optimization framework grounded in optimal transport. We derive an adaptive schedule that explicitly bounds the local Wasserstein distance between the discretized trajectory and the true continuous flow. We further introduce an *N-step resampling* procedure that projects this adaptive path onto a fixed NFE budget, allowing flexible control over the quality-efficiency trade-off.

Crucially, SDM is a *training-free* framework. It can be plugged into existing pre-trained diffusion models (e.g., EDM, Stable Diffusion) to immediately improve the Pareto frontier of quality versus efficiency. We demonstrate that SDM achieves state-of-the-art performance across standard benchmarks, including an FID of 1.93 on CIFAR-10 and 1.98 on AFHQv2, surpassing established baselines that rely on static heuristics.

2. Preliminaries

2.1. Probability Flow ODE

Diffusion models is a generative model framework that gradually injects noise into data through a forward process and subsequently removes noise through a learned reverse process. The following generative process can be formulated as a stochastic differential equation (SDE) parameterized by a noise schedule, where $s(t)$ and $\sigma(t)$ denote the scale and noise term, respectively.

In addition to the stochastic reverse-time SDE, there exists a deterministic *probability flow ODE* that produces the same marginal distribution as the reverse SDE (Song et al., 2020):

$$dx = \left[\frac{\dot{s}(t)}{s(t)} x - s(t)^2 \dot{\sigma}(t) \sigma(t) \nabla_x \log p \left(\frac{x}{s(t)}; \sigma(t) \right) \right] dt. \quad (1)$$

Sampling from diffusion models is performed by discretizing this ODE into a finite number of steps from prior distribution at $t = T$ to the data distribution at $t = 0$ using numerical intergration methods.

2.2. Parameterizations

Since the introduction of diffusion models, various parameterizations of the model output have been proposed. x -prediction and ϵ -prediction formulation has first been introduced (Ho et al., 2020), where the later expressed as a reparameterization of the original training objective. Sal-

imans and Ho (Salimans & Ho, 2022) further proposed v -prediction, where the model predicts a linear combination of data and noise, improving stability and sample quality. Flow-based generative models (Albergo & Vanden-Eijnden, 2022; Lipman et al., 2022; Liu et al., 2022) can also be interpreted within the v -prediction model framework, and recent work has actively explored the connection between diffusion models and flow-based formulations (Esser et al., 2024; Lipman et al., 2022).

Despite the popularity of alternative parameterizations, recent work (Li & He, 2025) has re-emphasized the importance of x -prediction, stating that directly predicting the clean image is more suitable for modeling low-dimensional manifolds embedded in high-dimensional space. This motivates us to reconsider the design space of EDM (Karras et al., 2022), which establishes a strong baseline by incorporating x -prediction formulation for training and sampling with additional pre-conditioning scheme.

2.3. Numerical Integration and Scheduling

Solving Equation (1) requires discretizing the time interval $[0, T]$ into a sequence $\{t_i\}_{i=0}^N$. The sample quality is governed by two coupled design choices: numerical solver and timestep schedules.

Numerical Solvers. Solvers navigate the trade-off between local precision and computational cost (NFE). First-order methods (e.g., Euler) are computationally cheap (1 NFE/step) but incur a local truncation error of $O(h^2)$. To improve precision without increasing steps, high-order solvers such as DPM-Solver++ (Lu et al., 2025), UniPC (Zhao et al., 2023), and DEIS (Zhang & Chen, 2022) employ higher-order Taylor approximations or predictor-corrector schemes. While these methods significantly reduce discretization error ($O(h^k)$ for $k \geq 2$), they typically require complex multi-step history or additional evaluations per step, making their uniform application across the entire trajectory potentially inefficient.

Timestep Scheduling. Diffusion timesteps $\{t_i\}_{i=0}^N$ determines the step size h_i and the noise levels $\sigma(t_i)$. Early works employed heuristic time-based schedules, such as linear (Ho et al., 2020) or cosine schedules (Nichol & Dhariwal, 2021). More recently, Karras et al. (Karras et al., 2022) proposed a noise-level based polynomial schedule (EDM), $\sigma_i = \left(\sigma_{\max}^{\frac{1}{\rho}} + \frac{i}{N-1} \left(\sigma_{\min}^{\frac{1}{\rho}} - \sigma_{\max}^{\frac{1}{\rho}} \right) \right)^{\rho}$, which has become a standard baseline due to its empirical robustness. Subsequent studies have explored timestep optimization based on various criteria including score-based measures (Williams et al., 2024; Xue et al., 2024), KL divergence (Sabour et al., 2024; Park et al., 2024; Li et al., 2023), and Wasserstein-based error estimates (Hu et al., 2024). However, there does not exist a unified framework that integrates solver

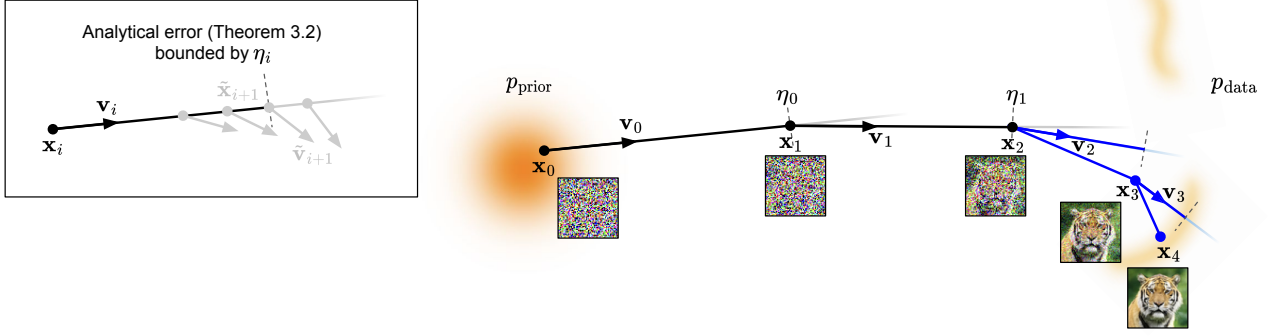


Figure 1. Overview of SDM. **(Inset)** We introduce an adaptive timestep optimization derived from an analytical upper bound on the Wasserstein error. Here, η_i serves as a controllable schedule that explicitly governs the allowable error budget at each step, tightening step sizes where the flow is most sensitive. **(Main)** Complementing this, SDM adapts the solver order to the trajectory’s geometry. In the early high-noise regime (black), the flow is nearly linear, allowing efficient low-order integration. As the trajectory approaches the data manifold (blue), the curvature increases, necessitating high-order solvers. These two strategies act as independent and complementary components, jointly improving both sample quality and computational efficiency.

selection and timestep allocation based on the intrinsic geometry of the diffusion trajectory. Motivated by this gap, we propose a unified sampling design space that characterizes both of these dimensions. Both components can be optimized independently for pre-trained diffusion models without additional training, while their combination yields further improvements in sampling efficiency and sample quality.

3. SDM: Sampling via Adaptive Solvers and Timestep Schedulers

We investigate the sampling design space of diffusion-based generative models by rigorously formalizing the trade-off between numerical precision and computational cost. While prior works often rely on static heuristics, we propose a geometric framework, *SDM*, which aligns the numerical solver with the intrinsic properties of the diffusion trajectory.

In Section 3.1, we analyze the local stiffness of the probability flow ODE. While state-of-the-art exponential integrators (e.g., DPM-Solver++ (Lu et al., 2025)) achieve efficiency by analytically solving the linear component of the diffusion ODE, they fundamentally rely on the assumption that the non-linear residual (the effective score term) varies smoothly. Our analysis generalizes this by explicitly quantifying the curvature of this residual, demonstrating that low-order solvers, such as Euler method, are sufficient for high-noise regimes, while higher-order corrections become necessary only in later stages. In Section 3.2, we introduce a Wasserstein-bounded adaptive strategy that optimizes the timestep schedule to minimize discretization error under a fixed computational budget. We empirically show that this leads to consistent improvements in sample quality.

3.1. Adaptive ODE Solvers

3.1.1. ANALYSIS OF ODE CURVATURE

To design an efficient adaptive sampling strategy, we must first quantify the geometric properties of the diffusion trajectory that govern numerical stability. The local truncation error (LTE) of any numerical solver is strictly bounded by the magnitude of the trajectory’s higher-order derivatives, specifically the acceleration $\|\ddot{x}\|$. This quantity serves as a direct proxy for the *local stiffness* of the probability flow ODE (Krämer & Hennig, 2024).

Exponential integrators mitigate stiffness by explicitly solving the linear drift term. However, the discretization error is then dominated by the higher-order derivatives of the neural network prediction itself (the non-linear noise residual). Our curvature analysis focuses on this residual complexity, providing a solver-agnostic measure of difficulty that applies regardless of the integrator’s baseline order.

In Theorem 3.1, we derive the closed-form expression of $\|\ddot{x}\|$ for standard diffusion parameterizations.

Theorem 3.1. *Under EDM/VP/VE parameterizations, the second derivative of the probability flow ODE can be expressed as follows:*

EDM

$$\ddot{x} = -\frac{1}{\sigma^2} J_D(x - D_\theta) - \frac{1}{\sigma} D_\sigma, \quad (2)$$

VP

$$\begin{aligned} \ddot{x} = & \left(\frac{1}{4} B^2 - \frac{1}{2} \beta_d \right) x + \left(\frac{\ddot{\sigma}}{\sigma} - B \frac{\dot{\sigma}}{\sigma} \right) (x - sD_\theta) \\ & - \dot{\sigma} \left(\frac{1}{2} B \frac{s}{\sigma^3} \right) J_D(x - sD_\theta) \\ & - \dot{\sigma} \left[\frac{s^2}{\sigma} \left(\frac{1}{4} B^2 - \frac{1}{2} \beta_d \right) \right] J_D D - \dot{\sigma} \left(\frac{\dot{\sigma} s}{\sigma} \right) D_\sigma, \end{aligned} \quad (3)$$

VE

$$\ddot{x} = -\frac{1}{4\sigma^4}(I + J_D)(x - D_\theta) - \frac{1}{4\sigma^3}D_\sigma, \quad (4)$$

where J_D and D_σ denote the Jacobian with respect to x and the partial derivative with respect to σ , respectively. Detailed proof and closed-form expressions for $B(t)$, $\dot{\sigma}(t)$, and $\ddot{\sigma}(t)$ under the VP formulation are provided in Appendix A.

The analytical forms in (2)–(4) imply that the probability flow is nearly linear during the early high-noise stages. However, its curvature increases rapidly as the process approaches the data manifold ($t \rightarrow 0$). This theoretical insight motivates the use of a mixed-solver strategy that progressively adapts the solver order to the trajectory's changing stiffness.

3.1.2. MIXTURE OF EULER/HEUN SOLVERS

While Theorem 3.1 highlights the varying stiffness across the diffusion trajectory, utilizing this insight requires a practical metric to allocate solver types efficiently. Computing the exact second derivative $\|\ddot{x}\|$ involves Hessian-vector products, which are computationally prohibitive to evaluate repeatedly. To address this, we introduce efficient discrete proxies based on the vector field variation, allowing us to construct an optimized solver schedule that adapts to the trajectory's geometry without incurring additional computational overhead during inference.

Given diffusion timesteps $\{t_i\}_{i=0}^N$ such that

$$t_0 > t_1 > \dots > t_N = 0, \quad (5)$$

let $v_i := v(x_i, t_i)$ denote the vector field evaluated at the (x_i, t_i) . We define the *absolute local curvature*¹ as

$$\kappa_{\text{abs}}(i) := \frac{\|v_{i+1} - v_i\|}{\Delta t_i} \approx \|\ddot{x}_i\|, \quad (6)$$

where $\Delta t_i = t_i - t_{i+1}$. To provide a scale-invariant measure of stiffness relative to the signal magnitude, we further introduce the *relative local curvature*,

$$\kappa_{\text{rel}}(i) := \frac{\kappa_{\text{abs}}(i)}{\|v_i\|}. \quad (7)$$

Computing $\kappa_{\text{rel}}(i)$ directly requires evaluating the vector field at both (x_i, t_i) and (x_{i+1}, t_{i+1}) , which increases twice the number of function evaluations (NFE), although using low-order solvers such as Euler method.

To avoid this overhead, we hence propose a *cache-based curvature* that does not require additional network evaluations.

¹In this work, we use the term ‘curvature’ to refer to the trajectory non-linearity (acceleration $\|\ddot{x}\|$) that dictates the truncation error of ODE solvers, following the convention in diffusion literature (Karras et al., 2022).

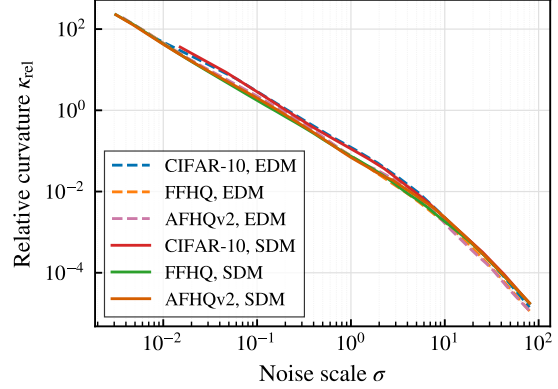


Figure 2. Relative curvature $\hat{\kappa}_{\text{rel}}$ as a function of noise level σ for standard benchmarks. The curvature exhibits an approximately linear correlation with noise levels σ in log scale, consistent with the theoretical derivation of second order probability flow ODE.

Specifically, we define

$$\hat{\kappa}_{\text{rel}}(i) := \frac{\|v_i - v_{i-1}\|}{\Delta t_i \|v_{i-1}\|}. \quad (8)$$

Since v_{i-1} is computed at the previous timestep and v_i is required for the current update, the curvature $\hat{\kappa}_{\text{rel}}(i)$ can be obtained by simply reusing the cached evaluations, resulting in $\text{NFE} = 1$ per step. A detailed analysis justifying that $\hat{\kappa}_{\text{rel}}(i)$ provides a consistent approximation of the relative local curvature is given in Appendix B.

We validate the theoretical findings of Theorem 3.1 across standard benchmarks by visualizing the log correlation between $\hat{\kappa}_{\text{rel}}(i)$ and noise levels, as shown in Figure 2.

Motivated by this curvature profile, we introduce a dynamic scheduling function $\Lambda(t) \in [0, 1]$ that controls the convex combination of a first-order Euler output $x^E(t)$ and a second-order Heun output $x^H(t)$:

$$x(t) = \Lambda(t)x^E(t) + (1 - \Lambda(t))x^H(t). \quad (9)$$

We consider step, linear, and cosine (Nichol & Dhariwal, 2021) scheduling functions for $\Lambda(t)$. For the step scheduler, we introduce threshold τ_k that determines when to switch from Euler to Heun updates based on the curvature measure.

3.2. Adaptive Timestep Schedulers

3.2.1. ADAPTIVE STEP SIZE BASED ON WASSERSTEIN DISTANCE

Given two probability distributions μ and ν , the squared 2-Wasserstein distance is defined as:

$$W_2^2(\mu, \nu) := \inf_{\pi \in \Pi(\mu, \nu)} \mathbb{E}_{(X, Y) \sim \pi} [\|X - Y\|^2], \quad (10)$$

where $\Pi(\mu, \nu)$ denotes the set of all couplings between μ and ν .

In diffusion-based generative models, each numerical integration step induces a transport between probability distributions at adjacent timesteps. Within this framework, the step size directly controls the local Wasserstein distance induced by the sampler.

Driven by this insight, we propose an *adaptive step size scheduling algorithm* that explicitly bounds the local Wasserstein distance at each sampling step.

Theorem 3.2 (Step Size with Local Wasserstein Bound). *Let Δt denote the step size at time t . The maximum step size that does not exceed the given the upper bound of the Wasserstein distance, denoted as η , can be derived as*

$$\Delta t \leq \sqrt{\frac{2\eta}{S_t}}, \quad (11)$$

where

$$S_t = \left(\mathbb{E} \left[\sup_{s \in [t, t + \Delta t]} \left\| \frac{d}{ds} v(x^*(s), s) \right\|^2 \right] \right)^{1/2}. \quad (12)$$

A detailed proof is provided in Appendix C.1.

The quantity S_t can be interpreted as the local variation of the velocity field along the true trajectory $x^*(s)$ over $[t, t + \Delta t]$. Since the following term is intractable, we approximate it by computing the velocity field of the intermediate step $t + \Delta t_{\text{trial}} \in [t, t + \Delta t]$ along the sampling trajectory.

$$\hat{S}_t := \left\| \frac{d}{dt} (v(x(t), t)) \right\| = \frac{\|v_{t + \Delta t_{\text{trial}}} - v_t\|}{\Delta t_{\text{trial}}}. \quad (13)$$

We denote the term as \hat{S}_t throughout the paper.

Theorem 3.3 (Total Wasserstein Distance Bound). *Let $\{t_i\}_{i=0}^N$ be discretized timesteps with step size $\Delta t_i = t_i - t_{i+1}$. Assume the velocity field $v(x, t)$ satisfies local Lipschitz conditions. Then, if we follow the adaptive step schedule defined in Equation (11), the total Wasserstein distance between the true distribution $p_{t_0}^*$ and its Euler approximation $p_{t_0}^E$ satisfies*

$$W_2(p_{t_N}^*, p_{t_N}^E) \leq e^{Lt_0} \sum_{i=0}^{N-1} \frac{\Delta t_i^2}{2} \bar{M}_i, \quad (14)$$

where

$$\bar{M}_i := \sup_{s \in [t_i, t_{i+1}]} M_s, \quad M_t := \left\| \frac{d}{dt} v(x(t), t) \right\|, \quad (15)$$

and L denotes the Lipschitz constant of the Euler transport map.

As stated in Theorem 3.3, we further show that taking the following step size consequently bounds the total Wasserstein

Algorithm 1 Adaptive Timestep Scheduling

Input: initial (\mathbf{x}_0, t_0) , model \mathbf{v}_{ϕ^\times} , error tolerance map η
 $i \leftarrow 0$
 $\mathbf{v}_0 \leftarrow \mathbf{v}_{\phi^\times}(\mathbf{x}_0, t_0)$
while $t_i > 0$ **do**
 $\tilde{t}_{i+1} \leftarrow \text{NEXTTimestep}(t_i)$
 repeat
 $\tilde{\mathbf{x}}_{i+1} \leftarrow \mathbf{x}_i - (t_i - \tilde{t}_{i+1}) \mathbf{v}_i$
 $\tilde{\mathbf{v}}_{i+1} \leftarrow \mathbf{v}_{\phi^\times}(\tilde{\mathbf{x}}_{i+1}, \tilde{t}_{i+1})$
 $\hat{S}_{t_i} \leftarrow \frac{\|\tilde{\mathbf{v}}_{i+1} - \mathbf{v}_i\|}{\tilde{t}_{i+1} - t_i}$ \triangleright Equation (13)
 $\tilde{t}_{i+1} \leftarrow \text{LINESEARCH}(\hat{S}_{t_i}, \tilde{t}_{i+1}, t_i)$
 until no further change in \tilde{t}_{i+1}
 $\Delta t \leftarrow \sqrt{\frac{2\eta(t_i)}{\hat{S}_{t_i}}} \triangleright$ Maximum step using Theorem 3.2
 $t_{i+1} \leftarrow t_i - \Delta t$
 $\mathbf{x}_{i+1} \leftarrow \mathbf{x}_i - \Delta t \mathbf{v}_i$
 $\mathbf{v}_{i+1} \leftarrow \mathbf{v}_{\phi^\times}(\mathbf{x}_{i+1}, t_{i+1})$
 $i \leftarrow i + 1$
end while
Output: $\{t_i\}$

distance by extending the analytical proof from AdaFlow (Hu et al., 2024) to score-based diffusion framework. The proof is provided in Appendix C.2.

Algorithm. The practical realization of our Wasserstein-bounded scheduling, summarized in Algorithm 1, adopts a computationally efficient predictor-corrector strategy to strictly enforce the local error bound derived in Theorem 3.2. To mitigate the computational cost of exhaustive search, the NEXTTimestep routine initializes the candidate \tilde{t}_{i+1} from a pre-defined reference grid, effectively warm-starting the search procedure with a value proximal to the optimal solution. This candidate is then verified against the theoretical maximum step size derived in Equation (11). If the candidate violates this bound or, conversely, proves overly conservative, the LINESEARCH routine refines the step size using an *exponential backoff mechanism*. By expanding or contracting the step size via multiplicative factors, this procedure ensures logarithmic convergence complexity $O(\log \frac{\Delta t}{\delta})$ akin to classical backtracking methods like the Armijo-Wolfe conditions (Armijo, 1966; Wolfe, 1969; 1971).

η -scheduling. In practice, the difficulty of the sampling dynamics varies significantly across noise levels. To account for this, we allow the error tolerance term η to depend on the current noise level σ as the following:

$$\eta_{\text{target}} = (\eta_{\max} - \eta_{\min}) \left(\frac{\sigma}{\sigma_{\max}} \right)^p + \eta_{\min}, \quad (16)$$

where $p \geq 0$ controls how strongly the error budget is concentrated throughout different noise levels. The following design assigns a larger tolerance during the early, high-noise

stages, while the error bound becomes more restrictive as $\sigma \rightarrow 0$.

3.2.2. N -STEP RESAMPLING

The proposed scheduling method provides a sequence of diffusion timesteps where the local Wasserstein distance is below a certain threshold value. However, the number of produced steps cannot be controlled. Hence, we propose an additional algorithm, where we resample given the number of steps we would like to take.

Given a sequence of diffusion timesteps $\{t_i\}_{i=0}^N$ and corresponding noise levels $\{\sigma_i\}_{i=0}^N$, defined by scheduler σ such that $t_i = \sigma^{-1}(\sigma_i)$, we define an incremental cost function $L(t_i, t_{i+1})$ and define the total cost and geodesic path length as

$$L = \sum_{i=0}^{N-1} L(t_i, t_{i+1}), \quad \Gamma = \sum_{i=0}^{N-1} \sqrt{L(t_i, t_{i+1})}. \quad (17)$$

As shown in prior work (Williams et al., 2024), the schedule that minimizes the corresponding energy function traverses the diffusion path at constant geodesic speed, i.e.,

$$\sqrt{L(t_i^*, t_{i+1}^*)} \approx \Gamma/N, \quad i = 0, \dots, N-1, \quad (18)$$

which implies that optimal timesteps can be obtained by uniformly discretizing the cumulative geodesic length Γ , which motivates our resampling procedure.

We show that the same conclusion holds and expand the following resampling procedure under a weighted incremental cost setting, as proven in Proposition C.1.

$$\tilde{L}(t_i, t_{i+1}) := w(t_i)L(t_i, t_{i+1}), \quad w(t) \geq 0. \quad (19)$$

Hence, we define our *weighted* incremental cost function using the empirically measured local error proxy η_i as

$$\tilde{L}(t_i, t_{i+1}) := w(t_i)\eta_i, \quad (20)$$

and correspondingly define the cumulative (weighted) geodesic length as

$$\tilde{\Gamma}(t_i) := \sum_{j=0}^{i-1} \sqrt{\tilde{L}(t_j, t_{j+1})} = \sum_{j=0}^{i-1} \sqrt{w(t_j)} \sqrt{\eta_j}. \quad (21)$$

We then obtain an N -step schedule by uniformly discretizing $\tilde{\Gamma}$ by selecting timesteps $\{t_i^*\}_{i=0}^N$ such that $\tilde{\Gamma}(t_i^*)$ is approximately linear in i , which we denote the following procedure as the *N -step resampling algorithm*.

In our implementation, we define the weighted function in terms of the noise level σ as

$$g(\sigma) := \left(\frac{\sigma}{\sigma_{\max}} \right)^{-q}, \quad w(t_i) = g(\sigma_i)^2, \quad (22)$$

where parameter $q \geq 0$ controls the degree of emphasis on the later steps. Larger values of q allocate a greater fraction of the sampling budget to the low- σ regime.

4. Experiments

4.1. Implementation Details

Datasets, Models, and Metrics. We evaluate our proposed SDM sampler on CIFAR-10 at 32×32 resolution, and FFHQ, AFHQv2, and ImageNet 64×64 resolution, following the baseline (Karras et al., 2022). We use pretrained models from EDM (Karras et al., 2022) with no additional training. We use FID and NFE to measure sample quality and sampling efficiency.

Baselines We follow the baseline timestep discretization from EDM schedule, where the noise levels $\{\sigma_i\}_{i=0}^N$ are defined as

$$\sigma_{i < N} = \left(\sigma_{\max}^{\frac{1}{\rho}} + \frac{i}{N-1} (\sigma_{\min}^{\frac{1}{\rho}} - \sigma_{\max}^{\frac{1}{\rho}}) \right)^{\rho}, \quad \sigma_N = 0. \quad (23)$$

with $\rho = 7$. We use a fixed number of timesteps for each dataset: 18 steps for CIFAR-10, 40 steps for FFHQ and AFHQv2, and 256 steps for ImageNet. We adopt stochastic settings with $S_{\text{churn}} = 40$, $S_{\min} = 0.05$, $S_{\max} = 50$, and $S_{\text{noise}} = 1.003$ for ImageNet.

For baseline comparisons, we evaluate both EDM and Corrector Optimized Schedules (Williams et al., 2024), which we abbreviate as COS throughout the paper. COS schedules are computed with batch size of 128.

ODE Solvers and Timestep Scheduling. For adaptive solvers, we experiment with step, linear, and cosine (Nichol & Dhariwal, 2021) schedules for our choice of $\Lambda(t)$. We apply adaptive scheduling to both Euler and Heun solvers. When using adaptive scheduling, we remove the stochastic settings from EDM, and use deterministic configurations for ImageNet.

Hyperparameters. We set the threshold term τ_k for step scheduler, Wasserstein error tolerance parameters η_{\min} , η_{\max} , p , and N -step resampling parameter q as our hyperparameters.

4.2. Results

Unconditional Generation. Quantitative results for unconditional generation are reported in Table 1. Across all datasets, solvers, and pre-trained model configurations, SDM consistently improves sample quality over prior baselines, demonstrating robust performance under both VP and VE parameterizations.

Under the Euler solver, SDM with adaptive scheduling yields substantial gains, achieving FID 6.18 on CIFAR-10, 4.16 on FFHQ, and 2.71 on AFHQv2 for VP models, compared to 7.61, 4.59, and 2.93 obtained by the EDM baseline, respectively. Similar improvements are observed for VE models. With the Heun solver, SDM remains competitive

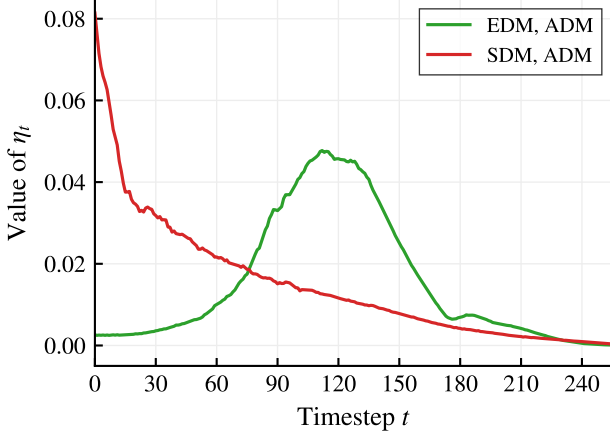


Figure 3. Distribution of local Wasserstein error bound η_t over diffusion timesteps for ImageNet 64×64 . EDM schedules exhibit an initially increasing trend with a subsequent decay, reaching maximum during the intermediate sampling stages. In contrast, SDM schedules allocate a larger portion of the error budget to the early high-noise stages, resulting in improved sample quality.

or superior to existing methods, e.g., achieving FID 2.41 on FFHQ and 2.13 on AFHQv2.

Applying the adaptive solver alone surpasses EDM baseline with Heun solvers, achieving FID 1.93 on CIFAR-10, 2.58 on FFHQ, and especially reducing the number of function evaluations (NFE) by approximately 15–20% while achieving FID 1.98 on AFHQv2. Increasing the threshold τ_k can further reduce NFE, enabling a flexible trade-off between sample quality and computational efficiency. Most notably, combining both adaptive solver with adaptive scheduling yields the best overall performance, reaching FID 1.97 for VP and 1.99 for VE configuration on AFHQv2.

Conditional Generation. Results for conditional generation are shown in Table 4. Under the Euler solver, SDM with adaptive scheduling achieves strong gains, obtaining state-of-the-art FID 6.10 and 5.12 on CIFAR-10 with VP and VE based models, respectively, and 2.32 on ImageNet.

For adaptive solver settings, SDM further improves both sample quality and sampling efficiency, achieving FID 1.81 and 1.77 on CIFAR-10 with VP and VE based models, respectively, and 1.45 on ImageNet. Adding the adaptive solver on top of adaptive scheduling yields further performance improvements compared to adaptive scheduling alone, indicating that the two components are complementary and can be effectively combined.

Further qualitative results are shown in Appendix E.

4.3. Ablation Studies

We conduct ablation studies on the following key components of the proposed SDM sampler.

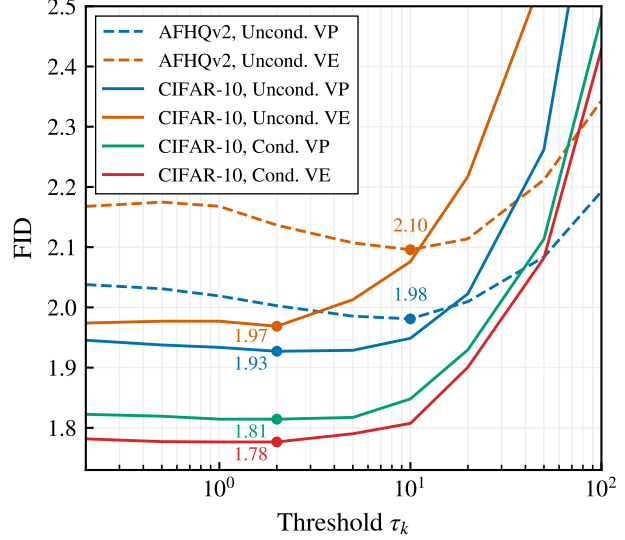


Figure 4. Ablation on threshold τ_k . FID as a function of the curvature threshold τ_k for CIFAR-10 (32×32 , solid) and AFHQv2 (64×64 , dashed), evaluated under unconditional and conditional settings using the step-scheduler-based adaptive solver. Markers denote the selected τ_k values that yield the best model performance for each dataset and training configuration.

Threshold τ_k . Under the step scheduling function $\Lambda(t)$, we investigate the effect of the threshold parameter τ_k , which controls the activation of higher order solvers. We evaluate FID while varying τ_k for each dataset, as shown in Figure 4. Based on the results, we set $\tau_k = 2 \times 10^{-4}$ for CIFAR-10, $\tau_k = 1 \times 10^{-4}$ for FFHQ and ImageNet, and $\tau_k = 1 \times 10^{-3}$ for AFHQv2 under EDM schedules. For SDM schedules, we further adjust the threshold on AFHQv2, using $\tau_k = 2 \times 10^{-4}$ for VP parameterization. Note that as long as $\tau_k > 0$, the number of function evaluation is less than 2 per diffusion timestep, *i.e.*, $\text{NFE} < 2$.

Choice of $\Lambda(t)$. We compare step, linear, and cosine schedules for the scheduler function $\Lambda(t)$. For step schedules, FID values are reported based on the optimized τ_k value selected above. Quantitative results are summarized in Table 5. Across all datasets and model configurations, step schedule consistently achieves the best FID performance. In addition, step schedules require fewer function evaluations per timestep with $\text{NFE} < 2$, whereas linear and cosine schedules require $\text{NFE} = 2$ per timestep.

Error tolerance and N -step resampling parameters. For adaptive scheduling, we perform a grid search over the error tolerance and resampling parameters on CIFAR-10, as detailed in Table 3. For the remaining datasets, we observe that performance is largely insensitive to the parameters. Consequently, we set parameters $\eta_{\min} = 0.02$, $\eta_{\max} = 0.20$, $p = 1.0$, and $q = 0.25$ for FFHQ and AFHQv2, and $\eta_{\min} = 0.001$, $\eta_{\max} = 0.01$, $p = 1.0$, and $q = 0.25$ for ImageNet.

Table 1. Quantitative results on unconditional generation for CIFAR-10 32×32 , FFHQ 64×64 , and AFHQv2 64×64 , measured by FID and NFE. Results for the adaptive solver are based on the step scheduling function $\Lambda(t)$ with the optimal threshold parameter τ_k . Adaptive scheduling is applied to Euler, Heun, and SDM-based adaptive solvers. The best-performing configurations compared to the corresponding baselines are highlighted in **bold**, while the overall best results across all methods are highlighted in **bold**. Overall, the proposed SDM sampler achieves superior performance in both sample quality and computational efficiency over all baselines.

Solver	Schedule	Unconditional CIFAR-10 32×32		Unconditional FFHQ 64×64		Unconditional AFHQv2 64×64	
		VP	VE	VP	VE	VP	VE
		7.61	7.75	4.59	4.76	2.93	3.21
Euler	EDM ($\rho = 7$)	7.43	7.25	4.29	4.46	2.89	3.10
	COS (Williams et al., 2024)	6.18	6.48	4.16	4.51	2.71	2.97
	NFE	17	17	39	39	39	39
Heun	EDM ($\rho = 7$)	1.96	1.97	2.47	2.59	2.04	2.17
	COS (Williams et al., 2024)	2.08	2.10	2.48	2.61	2.04	2.16
	SDM (Adaptive Scheduling)	2.00	1.95	2.41	2.52	2.08	2.13
SDM	NFE	35	35	79	79	79	79
	EDM ($\rho = 7$)	1.93	1.97	2.48	2.58	1.98	2.10
	NFE	31	32	72	76	66	67
	SDM (Adaptive Scheduling)	1.93	1.97	2.47	2.58	1.97	1.99
	NFE	32	33	76	77	75	72

4.4. Analysis of η_t

We analyze the evolution of per-step error indicator η_t for both SDM schedules and EDM schedules. As shown in Figure 3, for EDM schedules, η_t initially increases during the early sampling stages and decreases afterwards, indicating that there exists unnecessary error budget expended during the intermediate stages, leaving room for additional improvement. In contrast, SDM schedules exhibit a monotonically decreasing trend in η_t throughout the sampling trajectory, suggesting that SDM schedules efficiently allocates more of the allowable error budget to the early stages of sampling, where dynamics are smoother, while enforcing tighter error control in later stage when the sampling trajectory becomes more nonlinear. As a result, SDM schedules achieve improved sample quality by devoting higher precision to the more critical stages of generation.

5. Conclusion

In this work, we introduce a sampling design space that improves both sample quality and sampling efficiency for pretrained diffusion-based generative models. By formulating the second-order behavior of the optimal sampling trajectory from the probability flow ODE, we observe that

the trajectory curvature remains negligible during the early sampling stage, which motivates the use of first-order ODE solvers in this regime, while reserving higher-order integration for later stages where the dynamics become more nonlinear. Based on this observation, we propose an adaptive solver that dynamically selects numerical solvers according to the local behavior of the sampling trajectory. In parallel, we introduce an adaptive scheduling method that optimizes diffusion timesteps based on a criterion derived from a Wasserstein distance upper bound. Across extensive experiments, we demonstrate that each component consistently improves sampling quality and computational cost. We believe that our proposed method provides a strong and flexible baseline for future research on efficient diffusion sampling, and that the underlying principles are broadly applicable to other diffusion-based generative models and domains.

Impact Statement

This paper presents work whose goal is to advance the field of Machine Learning. There are many potential societal consequences of our work, none of which we feel must be specifically highlighted here.

References

Albergo, M. S. and Vandenberghe, E. Building normalizing flows with stochastic interpolants. *arXiv preprint arXiv:2209.15571*, 2022.

Armijo, L. Minimization of functions having Lipschitz continuous first partial derivatives. *Pacific Journal of Mathematics*, 16(1):1–3, 1966.

Esser, P., Kulal, S., Blattmann, A., Entezari, R., Müller, J., Saini, H., Levi, Y., Lorenz, D., Sauer, A., Boesel, F., et al. Scaling rectified flow transformers for high-resolution image synthesis. In *Forty-first international conference on machine learning*, 2024.

Ho, J., Jain, A., and Abbeel, P. Denoising diffusion probabilistic models. *Advances in neural information processing systems*, 33:6840–6851, 2020.

Ho, J., Salimans, T., Gritsenko, A., Chan, W., Norouzi, M., and Fleet, D. J. Video diffusion models. *Advances in neural information processing systems*, 35:8633–8646, 2022.

Hu, X., Liu, Q., Liu, X., and Liu, B. Adaflow: Imitation learning with variance-adaptive flow-based policies. *Advances in Neural Information Processing Systems*, 37: 138836–138858, 2024.

Karras, T., Aittala, M., Aila, T., and Laine, S. Elucidating the design space of diffusion-based generative models. *Advances in neural information processing systems*, 35: 26565–26577, 2022.

Kim, D., Lai, C.-H., Liao, W.-H., Murata, N., Takida, Y., Uesaka, T., He, Y., Mitsufuji, Y., and Ermon, S. Consistency trajectory models: Learning probability flow ode trajectory of diffusion. *arXiv preprint arXiv:2310.02279*, 2023.

Krämer, N. and Hennig, P. Stable implementation of probabilistic ode solvers. *J. Mach. Learn. Res.*, 25(1), January 2024. ISSN 1532-4435.

Li, L., Li, H., Zheng, X., Wu, J., Xiao, X., Wang, R., Zheng, M., Pan, X., Chao, F., and Ji, R. Autodiffusion: Training-free optimization of time steps and architectures for automated diffusion model acceleration. In *Proceedings of the IEEE/CVF International Conference on Computer Vision*, pp. 7105–7114, 2023.

Li, T. and He, K. Back to basics: Let denoising generative models denoise. *arXiv preprint arXiv:2511.13720*, 2025.

Lin, C.-H., Gao, J., Tang, L., Takikawa, T., Zeng, X., Huang, X., Kreis, K., Fidler, S., Liu, M.-Y., and Lin, T.-Y. Magic3d: High-resolution text-to-3d content creation. In *Proceedings of the IEEE/CVF conference on computer vision and pattern recognition*, pp. 300–309, 2023.

Lipman, Y., Chen, R. T., Ben-Hamu, H., Nickel, M., and Le, M. Flow matching for generative modeling. *arXiv preprint arXiv:2210.02747*, 2022.

Liu, X., Gong, C., and Liu, Q. Flow straight and fast: Learning to generate and transfer data with rectified flow. *arXiv preprint arXiv:2209.03003*, 2022.

Lu, C., Zhou, Y., Bao, F., Chen, J., Li, C., and Zhu, J. Dpm-solver++: Fast solver for guided sampling of diffusion probabilistic models. *Machine Intelligence Research*, pp. 1–22, 2025.

Luo, S., Tan, Y., Huang, L., Li, J., and Zhao, H. Latent consistency models: Synthesizing high-resolution images with few-step inference. *arXiv preprint arXiv:2310.04378*, 2023.

Meng, C., Rombach, R., Gao, R., Kingma, D., Ermon, S., Ho, J., and Salimans, T. On distillation of guided diffusion models. In *Proceedings of the IEEE/CVF conference on computer vision and pattern recognition*, pp. 14297–14306, 2023.

Nichol, A. Q. and Dhariwal, P. Improved denoising diffusion probabilistic models. In *International conference on machine learning*, pp. 8162–8171. PMLR, 2021.

Park, Y.-H., Lai, C.-H., Hayakawa, S., Takida, Y., and Mitsufuji, Y. Jump your steps: Optimizing sampling schedule of discrete diffusion models. *arXiv preprint arXiv:2410.07761*, 2024.

Poole, B., Jain, A., Barron, J. T., and Mildenhall, B. Dreamfusion: Text-to-3d using 2d diffusion. *arXiv preprint arXiv:2209.14988*, 2022.

Rombach, R., Blattmann, A., Lorenz, D., Esser, P., and Ommer, B. High-resolution image synthesis with latent diffusion models. In *Proceedings of the IEEE/CVF conference on computer vision and pattern recognition*, pp. 10684–10695, 2022.

Sabour, A., Fidler, S., and Kreis, K. Align your steps: Optimizing sampling schedules in diffusion models. *arXiv preprint arXiv:2404.14507*, 2024.

Salimans, T. and Ho, J. Progressive distillation for fast sampling of diffusion models. *arXiv preprint arXiv:2202.00512*, 2022.

Singer, U., Polyak, A., Hayes, T., Yin, X., An, J., Zhang, S., Hu, Q., Yang, H., Ashual, O., Gafni, O., et al. Make-a-video: Text-to-video generation without text-video data. *arXiv preprint arXiv:2209.14792*, 2022.

Song, Y., Sohl-Dickstein, J., Kingma, D. P., Kumar, A., Ermon, S., and Poole, B. Score-based generative modeling through stochastic differential equations. *arXiv preprint arXiv:2011.13456*, 2020.

Song, Y., Dhariwal, P., Chen, M., and Sutskever, I. Consistency models. *arXiv preprint arXiv:2303.01469*, 2023.

Wang, F.-Y., Huang, Z., Bergman, A., Shen, D., Gao, P., Lingelbach, M., Sun, K., Bian, W., Song, G., Liu, Y., et al. Phased consistency models. *Advances in neural information processing systems*, 37:83951–84009, 2024.

Williams, C., Campbell, A., Doucet, A., and Syed, S. Score-optimal diffusion schedules. *Advances in Neural Information Processing Systems*, 37:107960–107983, 2024.

Wolfe, P. Convergence conditions for ascent methods. *SIAM Review*, 11(2):226–235, 1969.

Wolfe, P. Convergence conditions for ascent methods. ii: Some corrections. *SIAM Review*, 13(2):185–188, 1971.

Xue, S., Liu, Z., Chen, F., Zhang, S., Hu, T., Xie, E., and Li, Z. Accelerating diffusion sampling with optimized time steps. In *Proceedings of the IEEE/CVF Conference on Computer Vision and Pattern Recognition*, pp. 8292–8301, 2024.

Yang, L., Zhang, Z., Zhang, Z., Liu, X., Xu, M., Zhang, W., Meng, C., Ermon, S., and Cui, B. Consistency flow matching: Defining straight flows with velocity consistency. *arXiv preprint arXiv:2407.02398*, 2024.

Zhang, Q. and Chen, Y. Fast sampling of diffusion models with exponential integrator. *arXiv preprint arXiv:2204.13902*, 2022.

Zhao, W., Bai, L., Rao, Y., Zhou, J., and Lu, J. Unipc: A unified predictor-corrector framework for fast sampling of diffusion models. *Advances in Neural Information Processing Systems*, 36:49842–49869, 2023.

A. Derivation of ODE curvature

General PF-ODE second-order derivative. We consider the probability flow ODE (PF-ODE) formulation of diffusion models. Following (Song et al., 2020), the PF-ODE can be written as

$$dx = \left[\frac{\dot{s}}{s} x - s^2 \dot{\sigma} \sigma \nabla_x \log p(x; \sigma) \right] dt. \quad (24)$$

Using the x -prediction formulation, the score function is expressed as

$$\nabla_x \log p(x; \sigma) = \frac{D_\theta(x; \sigma) - x}{\sigma^2}, \quad (25)$$

which yields the equivalent ODE

$$\dot{x} = \frac{\dot{s}}{s} x + \frac{\dot{\sigma}}{\sigma} \left(x - s D_\theta(x; \sigma) \right). \quad (26)$$

Defining

$$A = \frac{\dot{s}}{s}, \quad \epsilon_\theta := \frac{x - s D_\theta(x; \sigma)}{\sigma}, \quad (27)$$

we obtain the following

$$\dot{x} = Ax + \dot{\sigma} \epsilon_\theta. \quad (28)$$

Derivation of $\dot{\epsilon}_\theta$. Recall from Equation (27) that

$$\epsilon_\theta = \frac{x - s D_\theta(x, \sigma)}{\sigma}, \quad N := x - s D_\theta(x, \sigma), \quad (29)$$

so that $\epsilon_\theta = N/\sigma$. Differentiating yields

$$\dot{\epsilon}_\theta = \frac{\dot{N}\sigma - N\dot{\sigma}}{\sigma^2} = \frac{\dot{N}}{\sigma} - \frac{\dot{\sigma}}{\sigma} \epsilon_\theta. \quad (30)$$

Next, differentiating $N = x - s D_\theta$ gives

$$\begin{aligned} \dot{N} &= \dot{x} - \dot{s} D_\theta - s \dot{D}_\theta \\ &= \dot{x} - \dot{s} D_\theta - s (J_D \dot{x} + D_\sigma \dot{\sigma}) \\ &= (I - s J_D) \dot{x} - \dot{s} D_\theta - s D_\sigma \dot{\sigma}, \end{aligned} \quad (31)$$

where $J_D := \nabla_x D_\theta(x, \sigma)$ and $D_\sigma := \partial_\sigma D_\theta(x, \sigma)$. Substituting Equation (31) into Equation (30) yields

$$\dot{\epsilon}_\theta = \frac{(I - s J_D) \dot{x} - \dot{s} D_\theta - s D_\sigma \dot{\sigma}}{\sigma} - \frac{\dot{\sigma}}{\sigma} \epsilon_\theta. \quad (32)$$

Using $\dot{x} = \frac{\dot{s}}{s} x + \dot{\sigma} \epsilon_\theta$ and the identity

$$(I - s J_D) x - s D_\theta = x - s J_D x - s D_\theta = \sigma \epsilon_\theta - s \sigma J_D \epsilon_\theta - s^2 J_D D_\theta, \quad (33)$$

we expand Equation (32) as

$$\begin{aligned} \dot{\epsilon}_\theta &= \frac{\dot{s}}{s \sigma} [(I - s J_D) x - s D_\theta] + \frac{\dot{\sigma}}{\sigma} (I - s J_D) \epsilon_\theta - \frac{\dot{\sigma}}{\sigma} \epsilon_\theta - \frac{\dot{s}}{\sigma} D_\theta - \frac{s \dot{\sigma}}{\sigma} D_\sigma \\ &= \frac{\dot{s}}{s} \epsilon_\theta - \left(\dot{s} + \frac{\dot{\sigma} s}{\sigma} \right) J_D \epsilon_\theta - \frac{\dot{s} s}{\sigma} J_D D_\theta - \frac{\dot{\sigma} s}{\sigma} D_\sigma. \end{aligned} \quad (34)$$

Derivation of \ddot{x} . Taking the time derivative yields the second-order ODE

$$\ddot{x} = \dot{A} x + A \dot{x} + \ddot{\sigma} \epsilon_\theta + \dot{\sigma} \dot{\epsilon}_\theta \quad (35)$$

$$= (\dot{A} + A^2) x + (A \dot{\sigma} + \ddot{\sigma}) \epsilon_\theta + \dot{\sigma} \dot{\epsilon}_\theta. \quad (36)$$

where the first-order derivative term is replaced using Equation (28).

Using $A = \dot{s}/s$, we have

$$\dot{A} + A^2 = \frac{\ddot{s}}{s}, \quad A\dot{\sigma} + \ddot{\sigma} = \ddot{\sigma} + \dot{\sigma}\frac{\dot{s}}{s}. \quad (37)$$

Substituting all terms, we obtain the general curvature expression

$$\ddot{x} = \frac{\ddot{s}}{s}x + (\ddot{\sigma} + 2\dot{\sigma}\frac{\dot{s}}{s})\epsilon_\theta - \dot{\sigma}(\dot{s} + \frac{\dot{\sigma}s}{\sigma})J_D\epsilon_\theta - \dot{\sigma}\frac{\dot{s}s}{\sigma}J_DD_\theta - \dot{\sigma}\frac{\dot{\sigma}s}{\sigma}D_\sigma. \quad (38)$$

A.1. EDM formulation

For EDM formulation (Karras et al., 2022), we set

$$\sigma(t) = t, \quad s(t) = 1. \quad (39)$$

Note that although EDM discretizes sampling timesteps based on ρ -schedule in the noise domain, the underlying probability flow ODE is parameterized directly by the noise level. Hence,

$$\dot{\sigma} = 1, \quad \ddot{\sigma} = 0, \quad \dot{s} = \ddot{s} = 0. \quad (40)$$

Substituting into Equation (38), the second derivative simplifies to

$$\ddot{x} = -\frac{1}{\sigma}(J_D\epsilon_\theta + D_\sigma) = -\frac{1}{\sigma^2}J_D(x - D_\theta) - \frac{1}{\sigma}D_\sigma. \quad (41)$$

A.2. VP formulation

For the VP formulation, we use the parameterization

$$\sigma(t) = \sqrt{e^{u(t)} - 1}, \quad s(t) = \frac{1}{\sqrt{1 + \sigma(t)^2}}, \quad u(t) = \frac{1}{2}\beta_d t^2 + \beta_{\min}t. \quad (42)$$

For simplicity, we define

$$B(t) := \dot{u}(t) = \beta_{\min} + \beta_d t, \quad \dot{B}(t) = \beta_d. \quad (43)$$

Since $1 + \sigma(t)^2 = e^{u(t)}$, substituting to Equation (42), we have

$$s(t) = \frac{1}{\sqrt{1 + \sigma(t)^2}} = e^{-u(t)/2}. \quad (44)$$

Derivatives of $\sigma(t)$. By differentiating $\sigma(t) = \sqrt{e^{u(t)} - 1}$, we obtain

$$\dot{\sigma}(t) = \frac{e^{u(t)}\dot{u}(t)}{2\sqrt{e^{u(t)} - 1}} = \frac{(1 + \sigma(t)^2)B(t)}{2\sigma(t)} = \frac{1}{2}B(t)(\sigma(t) + \sigma(t)^{-1}). \quad (45)$$

Hence, we derive the second derivative of $\sigma(t)$ as

$$\begin{aligned} \ddot{\sigma}(t) &= \frac{1}{2}\dot{B}(t)(\sigma + \sigma^{-1}) + \frac{1}{2}B(t)\frac{d}{dt}(\sigma + \sigma^{-1}) \\ &= \frac{1}{2}\beta_d(\sigma + \sigma^{-1}) + \frac{1}{2}B(t)\dot{\sigma}(t)(1 - \sigma^{-2}). \end{aligned} \quad (46)$$

Substituting $\dot{\sigma}$ from (46) gives

$$\dot{\sigma}(t) = \frac{1}{2}\beta_d(\sigma + \sigma^{-1}) + \frac{1}{4}B(t)^2(\sigma - \sigma^{-3}). \quad (47)$$

Derivatives of $s(t)$. Using $s(t) = e^{-u(t)/2}$, we directly obtain

$$\frac{\dot{s}(t)}{s(t)} = -\frac{1}{2}\dot{u}(t) = -\frac{1}{2}B(t), \quad (48)$$

hence

$$\dot{s}(t) = -\frac{1}{2}B(t)s(t). \quad (49)$$

Taking the second derivative gives

$$\begin{aligned} \ddot{s}(t) &= \frac{d}{dt} \left(-\frac{1}{2}B(t)s(t) \right) = -\frac{1}{2}\dot{B}(t)s(t) - \frac{1}{2}B(t)\dot{s}(t) \\ &= -\frac{1}{2}\beta_d s(t) + \frac{1}{4}B(t)^2 s(t), \end{aligned} \quad (50)$$

In other words,

$$\frac{\ddot{s}(t)}{s(t)} = \frac{1}{4}B(t)^2 - \frac{1}{2}\beta_d. \quad (51)$$

Substitution into Equation (38). Substituting Equation (48) to our general PF-ODE second order expression, we obtain the following two terms as

$$\ddot{\sigma}(t) + 2\dot{\sigma}(t)\frac{\dot{s}(t)}{s(t)} = \ddot{\sigma}(t) - B(t)\dot{\sigma}(t), \quad (52)$$

$$\dot{s}(t) + \frac{\dot{\sigma}(t)s(t)}{\sigma(t)} = s(t) \left(\frac{\dot{s}(t)}{s(t)} + \frac{\dot{\sigma}(t)}{\sigma(t)} \right) = \frac{1}{2}B(t)\frac{s(t)}{\sigma(t)^2}. \quad (53)$$

As a result, under VP parameterization we get

$$\begin{aligned} \ddot{x} &= \left(\frac{1}{4}B^2 - \frac{1}{2}\beta_d \right) x + \left(\frac{\ddot{\sigma}}{\sigma} - B\frac{\dot{\sigma}}{\sigma} \right) (x - sD_\theta) \\ &\quad - \dot{\sigma} \left(\frac{1}{2}B\frac{s}{\sigma^3} \right) J_D(x - sD_\theta) - \dot{\sigma} \left[\frac{s^2}{\sigma} \left(\frac{1}{4}B^2 - \frac{1}{2}\beta_d \right) \right] J_D D_\theta - \dot{\sigma} \left(\frac{\dot{\sigma}s}{\sigma} \right) D_\sigma, \end{aligned} \quad (54)$$

where $B(t) = \beta_{\min} + \beta_d t$ and $\dot{\sigma}, \ddot{\sigma}$ are defined in Equation (45), Equation (47), respectively.

A.3. VE formulation

For VE formulation,

$$\sigma(t) = \sqrt{t}, \quad s(t) = 1, \quad (55)$$

Hence,

$$\dot{\sigma} = \frac{1}{2\sqrt{t}} = \frac{1}{2\sigma}, \quad \ddot{\sigma} = \frac{d}{dt}(\frac{1}{2\sigma}) = \frac{d}{d\sigma}(\frac{1}{2\sigma})\dot{\sigma} = -\frac{1}{4\sigma^3}, \quad \dot{s} = \ddot{s} = 0. \quad (56)$$

Substituting into (38), we obtain

$$\ddot{x} = -\frac{1}{4\sigma^3}(\epsilon_\theta + J_D\epsilon_\theta + D_\sigma) = -\frac{1}{4\sigma^4}(I + J_D)(x - D_\theta) - \frac{1}{4\sigma^3}D_\sigma. \quad (57)$$

B. Justification of the Proxy Curvature Estimator $\hat{\kappa}_{\text{rel}}(i)$

Given the following definition of relative local curvature $\kappa_{\text{rel}}(i)$ and its corresponding estimator $\hat{\kappa}_{\text{rel}}(i)$:

$$\kappa_{\text{rel}}(i) := \frac{\|v_{i+1} - v_i\|}{\Delta t_i \|v_i\|}, \quad \hat{\kappa}_{\text{rel}}(i) := \frac{\|v_i - v_{i-1}\|}{\Delta \hat{t}_i \|v_{i-1}\|}, \quad (58)$$

we would like to prove the following equation

$$\kappa_{\text{rel}}(i-1) = \hat{\kappa}_{\text{rel}}(i). \quad (59)$$

In other words, $\hat{\kappa}_{\text{rel}}(i)$ is a one-step delayed evaluation of $\kappa_{\text{rel}}(i)$, hence being a valid estimator.

Specifically if we consider the case $S_{\text{churn}} = 0$ following the notation in (Karras et al., 2022), no intermediate perturbation is introduced, hence the sampler evaluates the drift term exactly at the grid points, i.e.,

$$\hat{x}_i = x_i, \quad \hat{t}_i = t_i. \quad (60)$$

Note that (\hat{x}_i, \hat{t}_i) denotes the actual evaluation point used by the EDM sampler to compute the velocity v_i . Hence, the corresponding velocity field evaluations are numerically identical:

$$v(\hat{x}_i, \hat{t}_i) = v(x_i, t_i) = v_i. \quad (61)$$

Moreover, since

$$\Delta\hat{t}_i = t_i - t_{i+1} = \Delta t_i \quad (62)$$

the effective step size also remains unchanged, hence the proof.

C. Additional Proofs

C.1. Proof of Theorem 3.2

We provide a detailed proof of Theorem 3.2, which establishes a sufficient condition on step size Δt such that the Wasserstein distance between the true diffusion trajectory and its numerical approximation remains bounded.

Let $x(t)$ denote the solution of the diffusion ODE driven by the velocity field $v(\cdot, \cdot)$. For a given time t , the exact state at time $t + \Delta t$ can be written as

$$x(t + \Delta t) = x(t) + \int_t^{t + \Delta t} v(x(\tau), \tau) d\tau. \quad (63)$$

Since the true velocity field along the true trajectory is generally intractable, we approximate the integral using a numerical solver. In particular, we consider the first-order Euler method:

$$x_E(t + \Delta t) = x(t) + \Delta t v(x(t), t). \quad (64)$$

The resulting discretization error is therefore

$$x(t + \Delta t) - x_E(t + \Delta t) = \int_t^{t + \Delta t} (v(x(\tau), \tau) - v(x(t), t)) d\tau. \quad (65)$$

Meanwhile, we define the auxiliary function

$$g(\tau) := v(x(\tau), \tau). \quad (66)$$

Then, by the fundamental theorem of calculus,

$$g(\tau) - g(t) = \int_t^\tau g'(s) ds, \quad (67)$$

which implies the bound

$$\|g(\tau) - g(t)\| \leq (\tau - t) \sup_{s \in [t, t + \Delta t]} \|g'(s)\|. \quad (68)$$

Substituting this bound into Equation (65) yields

$$\|x(t + \Delta t) - x_E(t + \Delta t)\| \leq \int_t^{t + \Delta t} (\tau - t) d\tau \sup_{s \in [t, t + \Delta t]} \left\| \frac{d}{ds} (v(x(s), s)) \right\| = \frac{\Delta t^2}{2} \sup_{s \in [t, t + \Delta t]} \left\| \frac{d}{ds} v(x(s), s) \right\|. \quad (69)$$

We now derive the discretization error in relation to the 2-Wasserstein distance. Recall the definition of Wasserstein distance between two probability measures μ and ν :

$$W_2(\mu, \nu)^2 = \inf_{\pi \in \Pi(\mu, \nu)} \mathbb{E}_{(X, Y) \sim \pi} [\|X - Y\|^2]. \quad (70)$$

Let $x_t \sim p_t$ denote the random variable following the diffusion trajectory at time t . We then define the coupled random variables

$$x_{t+\Delta t}^* = \Phi_{t+\Delta t}^*(x_t), \quad x_{t+\Delta t}^E = \Phi_{t+\Delta t}^E(x_t). \quad (71)$$

where $x_{t+\Delta t}^*$, $x_{t+\Delta t}^E$ corresponds to the exact and Euler-integrated flows, respectively.

Since the Wasserstein distance is upper bounded by the expected squared distance under any coupling, we obtain

$$W_2(p_{t+\Delta t}^*, p_{t+\Delta t}^E) \leq (\mathbb{E} [\|x_{t+\Delta t}^* - x_{t+\Delta t}^E\|^2])^{1/2} \leq \frac{\Delta t^2}{2} \left(\mathbb{E} \left[\sup_{s \in [t, t+\Delta t]} \left\| \frac{d}{ds} v(x^*(s), s) \right\|^2 \right] \right)^{1/2}. \quad (72)$$

Therefore, requiring the Wasserstein distance to be bounded by a specified tolerance η ,

$$W_2(p_{t+\Delta t}^*, p_{t+\Delta t}^E) \leq \eta, \quad (73)$$

leads to the following sufficient condition on the step size:

$$\Delta t \leq \sqrt{\frac{2\eta}{S_t}}, \quad (74)$$

where

$$S_t = \left(\mathbb{E} \left[\sup_{s \in [t, t+\Delta t]} \left\| \frac{d}{ds} v(x^*(s), s) \right\|^2 \right] \right)^{1/2}. \quad (75)$$

Hence, the proof.

C.2. Proof of Theorem 3.3

Here, we provide a complete proof of the total Wasserstein distance bound stated in Theorem 3.3.

Let $x(t)$ denote the solution of the probability flow ODE

$$\dot{x}(t) = v(x(t), t). \quad (76)$$

By the chain rule, the derivative of the velocity field along the trajectory is given by

$$\frac{d}{dt} v(x(t), t) = \partial_t v(x, t) + J_x v(x, t) \dot{x}(t). \quad (77)$$

Assume the velocity field satisfies the following local Lipschitz conditions:

$$\sup_x \|\partial_t v(x, t)\| \leq R_t, \quad \sup_x \|J_x v(x, t)\| \leq L, \quad \sup_x \|v(x, t)\| \leq V_t. \quad (78)$$

Then, we get

$$\left\| \frac{d}{dt} v(x(t), t) \right\| \leq R_t + L \|v(x(t), t)\| := M_t. \quad (79)$$

Let $p_{t+\Delta t}^*$ denote the true distribution at time $t + \Delta t$, and $p_{t+\Delta t}$ its Euler approximation. By substituting into Equation (72), we obtain the local Wasserstein distance bound as

$$W_2(p_{t+\Delta t}^*, p_{t+\Delta t}) \leq \frac{\Delta t^2}{2} \left(\mathbb{E} \left[\sup_{s \in [t, t+\Delta t]} \left\| \frac{d}{ds} v(x^*(s), s) \right\|^2 \right] \right)^{1/2} \leq \frac{\Delta t^2}{2} M_t. \quad (80)$$

Let

$$\mu_i := p_{t_i}^*, \quad \nu_i := p_{t_i}^E. \quad (81)$$

Define the exact flow operator Φ_i^* and Euler flow operator Φ_i^E such that

$$\mu_{i+1} = \Phi_i^*(\mu_i), \quad \nu_{i+1} = \Phi_i^E(\nu_i). \quad (82)$$

We introduce an auxiliary distribution

$$\tilde{\nu}_{i+1} := \Phi_i^E(\mu_i), \quad (83)$$

which corresponds to applying one Euler step starting from the true distribution. Hence, by the triangle inequality,

$$W_2(\mu_{i+1}, \nu_{i+1}) \leq W_2(\mu_{i+1}, \tilde{\nu}_{i+1}) + W_2(\tilde{\nu}_{i+1}, \nu_{i+1}). \quad (84)$$

The first term corresponds to the local truncation error:

$$\delta_i := W_2(\Phi_i^*(\mu_i), \Phi_i^E(\mu_i)) \leq \frac{\Delta t^2}{2} \bar{M}_i, \quad (85)$$

where $\bar{M}_i := \sup_{s \in [t_i, t_{i+1}]} M_s$.

For the second term, note that the Euler map

$$T_i(x) = x + \Delta t_i v(x, t_i), \quad (86)$$

is $(1 + \Delta t_i L)$ -Lipschitz. Therefore,

$$W_2(\tilde{\nu}_{i+1}, \nu_{i+1}) = W_2(\Phi_i^E(\mu_i), \Phi_i^E(\nu_i)) \leq (1 + \Delta t_i L) W_2(\mu_i, \nu_i). \quad (87)$$

Combining Equation (84) and Equation (85) yields the recursive inequality

$$W_2(\mu_{i+1}, \nu_{i+1}) \leq W_2(\Phi_i^*(\mu_i), \Phi_i^E(\nu_i)) + (1 + \Delta t_i L) W_2(\mu_i, \nu_i) = \delta_i + (1 + \Delta t_i L) W_2(\mu_i, \nu_i). \quad (88)$$

Unrolling the recursion gives

$$W_2(\mu_N, \nu_N) \leq \sum_{i=0}^{N-1} \left(\delta_i \prod_{j=i+1}^{N-1} (1 + \Delta t_j L) \right). \quad (89)$$

Using the inequality $1 + x \leq e^x$,

$$\prod_{j=i+1}^{N-1} (1 + \Delta t_j L) \leq \prod_{j=i+1}^{N-1} \exp(\Delta t_j L) \leq \exp \left(L \sum_{j=0}^{N-1} \Delta t_j \right) \leq \exp \left(L \sum_{j=0}^{N-1} \Delta t_j \right) = e^{L t_0}. \quad (90)$$

Hence, the upper bound of the total Wasserstein distance can be derived as

$$W_2(\mu_N, \nu_N) = W_2(p_{t_N}^*, p_{t_N}^E) \leq e^{L t_0} \sum_{i=0}^{N-1} \delta_i \leq e^{L t_0} \sum_{i=0}^{N-1} \frac{\Delta t_i^2}{2} \bar{M}_i, \quad (91)$$

which completes the proof.

C.3. Energy-Optimized Geodesic Path for Weighted Incremental Cost

Proposition C.1. *Assume the incremental cost admits the quadratic form*

$$L(t_i, t_{i+1}) \approx \delta(t_i) \Delta t_i^2, \quad \Delta t_i := t_i - t_{i+1}, \quad (92)$$

for some nonnegative function $\delta(\cdot)$. Then the weighted cost can be written as

$$\tilde{L}(t_i, t_{i+1}) \approx \tilde{\delta}(t_i) \Delta t_i^2, \quad \tilde{\delta}(t) := w(t) \delta(t). \quad (93)$$

Consequently, the optimal schedule for the weighted objective traverses the diffusion path a constant speed with respect to the weighted geodesic length

$$\tilde{\Gamma} := \sum_{i=0}^{N-1} \sqrt{\tilde{L}(t_i, t_{i+1})} = \sum_{i=0}^{N-1} \sqrt{w(t_i)} \sqrt{L(t_i, t_{i+1})}, \quad (94)$$

i.e.,

$$\sqrt{\tilde{L}(t_i, t_{i+1})} \approx \frac{\tilde{\Gamma}}{N}. \quad (95)$$

Proof. By Equation (19) and Equation (92),

$$\tilde{L}(t_i, t_{i+1}) = w(t_i)L(t_i, t_{i+1}) \quad (96)$$

$$\approx w(t_i)\delta(t_i)\Delta t_i^2 = \tilde{\delta}(t_i)\Delta t_i^2. \quad (97)$$

hence, the proof. The remainder follows by applying the same proof with δ replaced by $\tilde{\delta}$ (Williams et al., 2024). \square

D. Further Implementation Details

D.1. Hyperparameter Settings

We provide the search grids for hyperparameters used throughout our experiments. For the step schedule based adaptive solver, we vary the curvature threshold τ_k across datasets and timestep schedules. We observe that VP and VE models exhibit similar performance under the same threshold configuration on standard benchmarks, with the exception of AFHQv2, and therefore share the same τ_k values. For AFHQv2, we select $\tau_k = 2 \times 10^{-4}$ for VP parameterization and $\tau_k = 1 \times 10^{-3}$ for VE parameterization, which yields the best FID performance.

Table 2. Parameter search grid for threshold τ_k for step schedule based adaptive solver selection.

Timestep Schedule	CIFAR-10	FFHQ	AFHQv2	ImageNet	Grid search
EDM	2×10^{-4}	1×10^{-4}	1×10^{-3}	1×10^{-4}	$\{2, 5, 10, 20, 50, 100\} \times 10^{-5}$
SDM (Adaptive Scheduling)	2×10^{-4}	1×10^{-4}	2×10^{-4} (VP) 1×10^{-3} (VE)	1×10^{-4}	$\{2, 5, 10, 20, 50, 100\} \times 10^{-5}$

For adaptive timestep scheduling, we tune four hyperparameters, η_{\min} , η_{\max} , p , and q , which jointly control the overall Wasserstein error tolerance and its allocation across diffusion timesteps. We find that CIFAR-10 is relatively sensitive to the choice of these parameters, necessitating explicit tuning across different training configurations. In contrast, the remaining benchmarks (FFHQ, AFHQv2, and ImageNet) demonstrate robust performance across the hyperparameter grid.

Table 3. Parameter search grid for Wasserstein error tolerance and N -step resampling parameters for CIFAR-10.

Parameter	CIFAR-10				Grid search
	Uncond. VP	Uncond. VE	Cond. VP	Cond. VE	
η_{\min}	0.01	0.01	0.01	0.02	0.01, 0.02, 0.03, 0.04, 0.05
η_{\max}	0.40	0.40	0.40	0.10	0.10, 0.20, 0.30, 0.40, 0.50
p	1.0	1.0	1.0	1.0	0.8, 1.0, 1.2
q	0.1	0.25	0.1	0.25	0.1, 0.25

E. Additional Results

In this section, we provide additional results for our proposed SDM sampler.

E.1. Quantitative Results for Conditional Generation

Table 4. Quantitative results on conditional generation for CIFAR-10 32×32 and ImageNet 64×64 , measured by FID and NFE. Results for the adaptive solver are based on the step scheduling function $\Lambda(t)$ with the optimal threshold parameter τ_k . Adaptive scheduling is applied to Euler, Heun, and SDM-based adaptive solvers. The best-performing configurations compared to the corresponding baselines are highlighted in **bold**, while the overall best results across all methods are highlighted in **bold**. Overall, the proposed SDM sampler achieves superior performance in both sample quality and computational efficiency over all baselines.

Solver	Schedule	Conditional		Conditional
		CIFAR-10 32×32		ImageNet 64×64
		VP	VE	ADM
Euler	EDM ($\rho = 7$)	7.09	6.75	3.48
	COS (Williams et al., 2024)	7.05	6.66	3.74
	SDM (Adaptive Scheduling)	6.10	5.12	2.32
Heun	NFE	17	17	255
	EDM ($\rho = 7$)	1.82	1.78	1.45
	COS (Williams et al., 2024)	1.92	1.87	1.40
SDM	SDM (Adaptive Scheduling)	1.92	1.92	2.25
	NFE	35	35	511
	EDM ($\rho = 7$)	1.81	1.77	1.45
	NFE	30	32	476
	SDM (Adaptive Scheduling)	1.81	1.77	2.25
	NFE	32	33	503

E.2. Ablation Studies on $\Lambda(t)$

We provide a quantitative comparison among different choices of the scheduler function $\Lambda(t)$ when used with the proposed adaptive solver. As shown in Table 5, the step scheduler consistently achieves the best FID across all datasets and training configurations, while additionally requiring fewer function evaluations (NFE < 2) per diffusion timestep compared to linear and cosine schedules (NFE = 2). Based on these results, we adopt the step scheduler as the default choice in all experiments.

Table 5. Ablation Studies on scheduler function $\Lambda(t)$ for adaptive solvers. Step schedule consistently achieves the best FID across all datasets and model configurations, while additionally requiring lower NFE per diffusion timestep compared to other schedules.

$\Lambda(t)$	CIFAR-10 32×32				FFHQ 64×64		AFHQv2 64×64		ImageNet 64×64
	Unconditional		Conditional		Unconditional	Unconditional	Unconditional	Conditional	Conditional
$\Lambda(t)$	VP	VE	VP	VE	VP	VE	VP	VE	ADM
Step	1.93	1.97	1.81	1.77	2.48	2.58	1.98	2.17	1.45
Linear	2.73	2.90	2.61	2.46	3.13	3.35	2.21	2.39	1.69
Cosine	2.74	3.00	2.57	2.45	3.16	3.39	2.20	2.37	1.61

E.3. Qualitative Results

We present qualitative comparisons between the proposed SDM sampler and the baseline EDM sampler (Karras et al., 2022) across different datasets and training parameterizations.



Figure 5. Qualitative comparison on AFHQv2 (64×64) across VP (left) and VE (right) parameterizations. From top to bottom: EDM (Heun), SDM (adaptive solver), SDM (adaptive scheduling), and SDM (adaptive solver + scheduling). Each panel shows a 3×5 grid of generated samples; corresponding FID and NFE are reported below.



Figure 6. Qualitative comparison on FFHQ (64×64) across VP (left) and VE (right) parameterizations. From top to bottom: EDM (Heun), SDM (adaptive solver), SDM (adaptive scheduling), and SDM (adaptive solver + scheduling). Each panel shows a 3×5 grid of generated samples; corresponding FID and NFE are reported below.

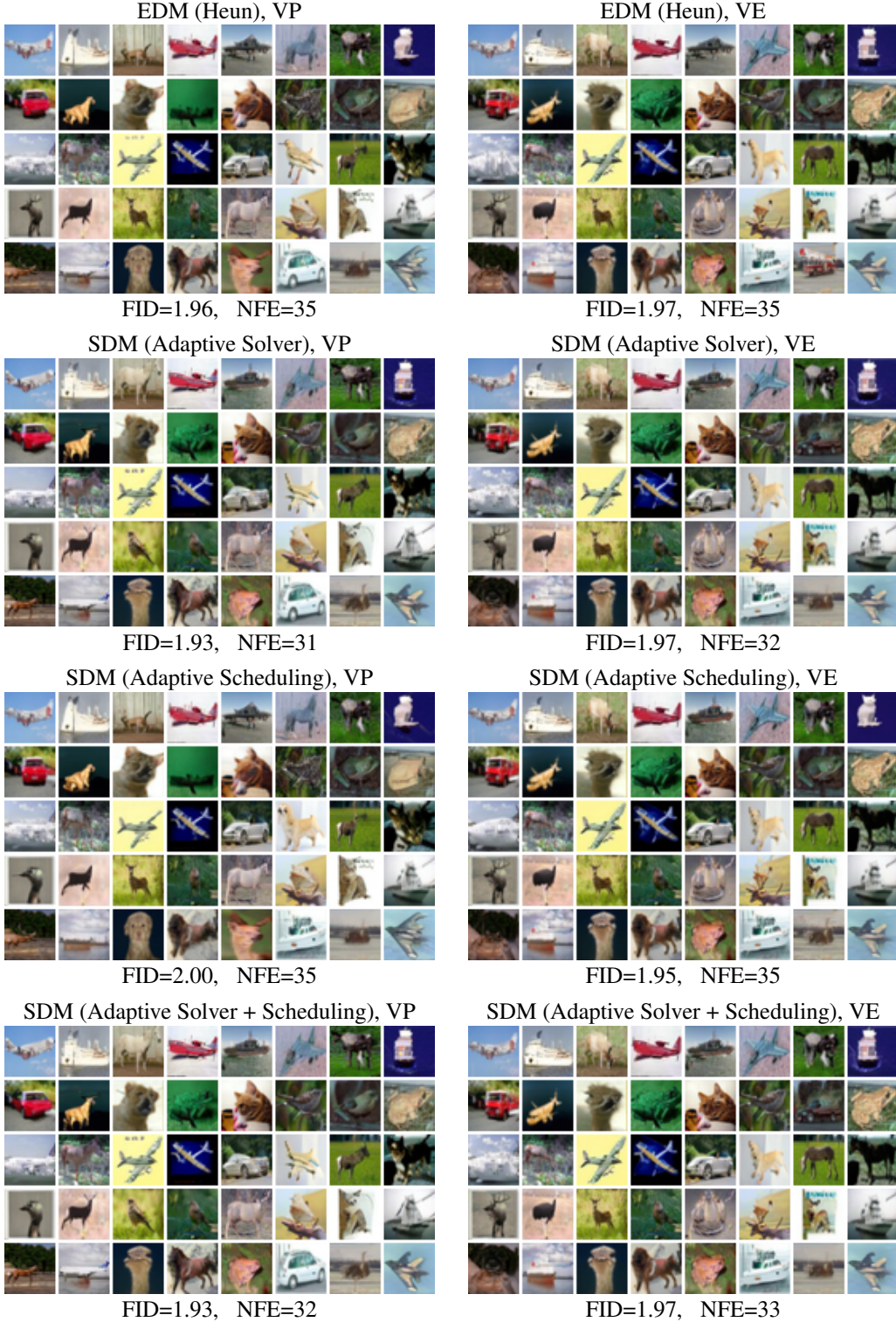


Figure 7. Qualitative comparison on unconditional generation for CIFAR-10 (32 \times 32) across VP (left) and VE (right) parameterizations. From top to bottom: EDM (Heun), SDM (adaptive solver), SDM (adaptive scheduling), and SDM (adaptive solver + scheduling). Each panel shows a 5 \times 8 grid of generated samples; corresponding FID and NFE are reported below.

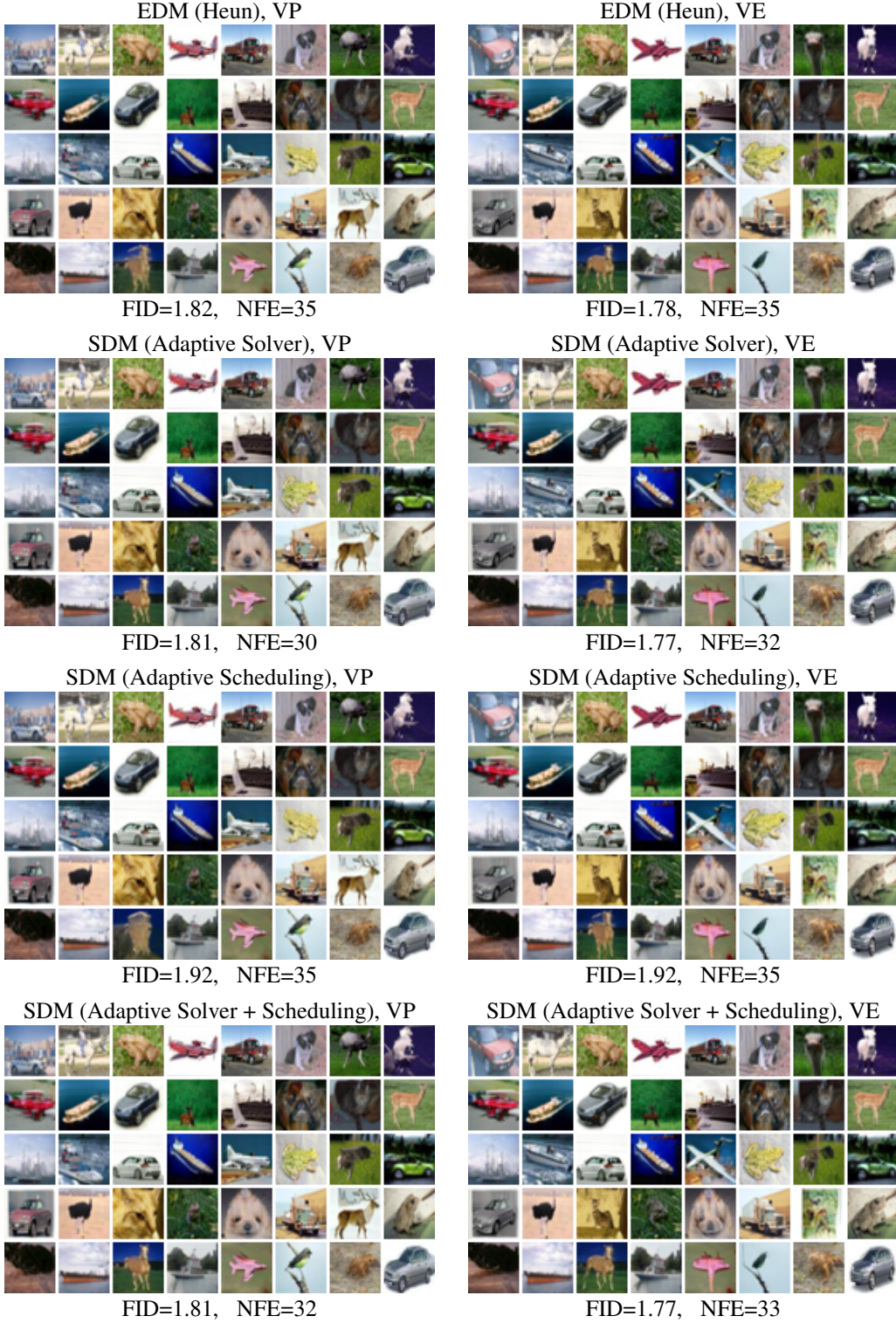


Figure 8. Qualitative comparison on conditional generation for CIFAR-10 (32 × 32) across VP (left) and VE (right) parameterizations. From top to bottom: EDM (Heun), SDM (adaptive solver), SDM (adaptive scheduling), and SDM (adaptive solver + scheduling). Each panel shows a 5 × 8 grid of generated samples; corresponding FID and NFE are reported below.

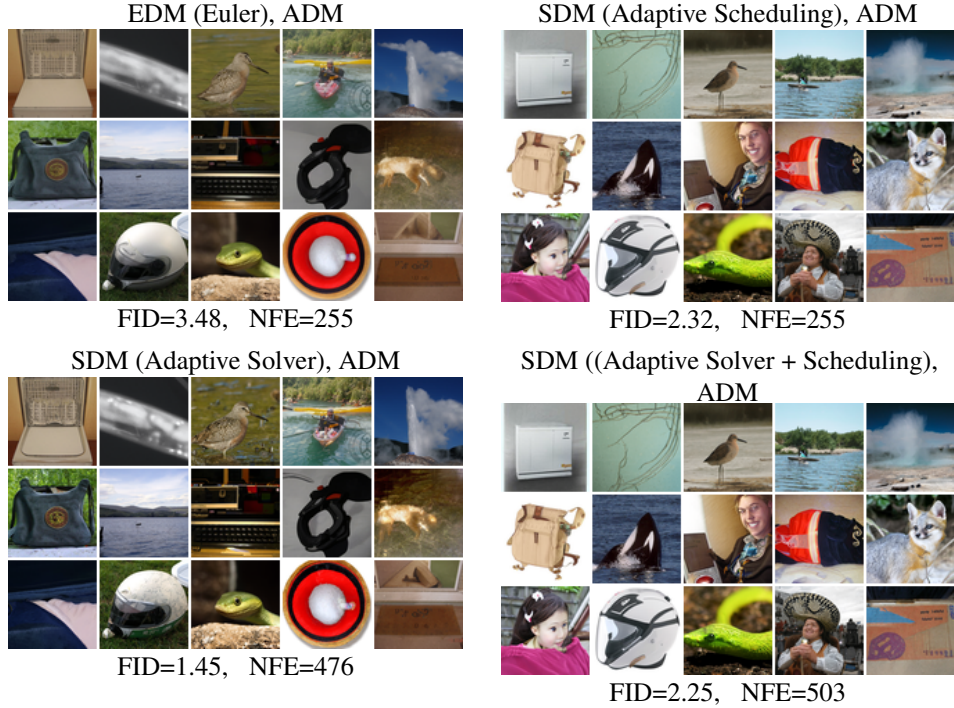


Figure 9. Qualitative comparison on ImageNet (64×64) under ADM parameterizations. From top left to bottom right: EDM (Heun), SDM (adaptive scheduling), SDM (adaptive solver), and SDM (adaptive solver + scheduling). Each panel shows a 3×5 grid of generated samples; corresponding FID and NFE are reported below.